ADVANCED ENERGY MATERIALS
www.advenergymat.de

# Amino-Arsine and Amino-Phosphine Based Synthesis of InAs@InP@ZnSe core@shell@shell Quantum Dots

*Zheming Liu, Jordi Llusar, Hiba H. Karakkal, Dongxu Zhu, Yurii P. Ivanov, Mirko Prato, Giorgio Divitini, Sergio Brovelli,* Ivan Infante,* Luca De Trizio,* and Liberato Manna**

**A colloidal synthesis protocol is demonstrated for InAs@InP core@shell quantum dots (QDs) with a tunable InP shell thickness (ranging from 3 to 8 monolayers), utilizing tris(diethylamino)-arsine and -phosphine. Structural analysis reveals that the InP shell preferentially grows onto the tetrahedral InAs cores along the <-1-1-1> directions, forming tetrapodal-shaped InAs@InP QDs. Growth of the InP shell causes a red shift in the absorption spectrum of the QDs. This is explained by considering that electrons are delocalized throughout the whole core@shell QDs, while holes preferentially leak along the <-1-1-1> directions, as indicated by the density functional theory calculations. This means such heterostructures cannot be described as type-I or quasi type-II, contrary to earlier assumptions. The overlap of carrier wavefunctions throughout the entire InAs@InP QD structure results in no significant reduction of the Auger recombination rate, which remains as fast as in InAs QDs. However, the InP shell enhances photoluminescence (PL) efficiency (up to ≈13%) by passivating surface trap states of the InAs QDs (mainly located close to the top of the valence band). The overgrowth of a ZnSe shell endows the QDs with a high PL efficiency (≈55%) and good stability upon air exposure (≈80% PL intensity retention after 14 days).**

## 1. Introduction

Colloidal quantum dots (QDs) that absorb and emit in the infrared (IR) region of the spectrum are attracting increasing interest as scalable and cost-effective building blocks for emerging optoelectronic technologies. In fact, IR QDs can be employed as active materials in solar concentrators, IR light-emitting diodes (LEDs), IR lasers, and sensors, which find applications in security authentication, optogenetics, crop life-cycle management, light fidelity, surveillance, automotive, night/cloud vision, object inspection, and optical communications.[1–10] Moreover, IR QDs are particularly suitable for in vivo bioimaging, biomedical sensing, and photodynamic therapy, since biological tissues, as well as oxygenated and deoxygenated blood, feature semi-transparency in specific IR regions.[9–11] The search for IR materials compliant with the Restriction of Hazardous Substances (RoHS) directive narrows down to a few candidates, including Ag- and Cu- based I-III-VI semiconductors (i.e., $CuInSe_2$, $CuInS_2$, and $AgInSe_2$), Ag chalcogenides, and InAs QDs.[12–15] Among these, InAs QDs stand out since their bandgap can be tuned from the visible range to ≈0.7 eV (corresponding to 1700 nm) through quantum confinement (i.e., size tuning), making them the

Z. Liu, D. Zhu, L. Manna
Nanochemistry, Istituto Italiano di Tecnologia
Via Morego 30, Genova 16163, Italy
E-mail: liberato.manna@iit.it
J. Llusar, I. Infante
BCMaterials, Basque Center for Materials, Applications, and Nanostructures
UPV/EHU Science Park
Leioa 48940, Spain
E-mail: ivan.infante@bcmaterials.net
H. H. Karakkal, S. Brovelli
Dipartimento di Scienza dei Materiali
Università degli Studi di Milano-Bicocca
Via R. Cozzi 55, Milano 20125, Italy
E-mail: sergio.brovelli@unimib.it
Y. P. Ivanov, G. Divitini
Electron Spectroscopy and Nanoscopy
Istituto Italiano di Tecnologia
Via Morego 30, Genova 16163, Italy
M. Prato
Materials Characterization
Istituto Italiano di Tecnologia
Via Morego 30, Genova 16163, Italy
I. Infante
Ikerbasque Basque Foundation for Science
Bilbao 48009, Spain
L. De Trizio
Chemistry Facility
Istituto Italiano di Tecnologia
Via Morego 30, Genova 16163, Italy
E-mail: luca.detrizio@iit.it

The ORCID identification number(s) for the author(s) of this article can be found under https://doi.org/10.1002/aenm.202402246



**DOI: 10.1002/aenm.202402246**

most promising and versatile candidates for commercial IR applications.[7,12–13,16–26]

One of the current main challenges of InAs QDs is the optimization of their photoluminescence (PL), both in terms of efficiency (i.e., quantum yield, QY) and non-radiative Auger recombination rate. The latter is an aspect that becomes relevant under continuous illumination conditions or under electrical injection (causing QD charging).[25,27–29] Indeed, QD emitters with suppressed Auger recombination are prime candidates for optical devices like LEDs and lasers.[30,31] Despite considerable advances in controlling the size and size distribution of InAs QDs in recent years,[23,25,32,33] their PL, particularly at wavelengths longer than 1200 nm, remains weak.[25,34,35] The most effective approach to increase the PLQY of InAs QDs involves their encapsulation in suitable wide bandgap shell materials.[7,29,35–44] Excluding Cd-based chalcogenides due to toxicity reasons, options are limited to ZnSe and/or ZnS. Both of them have much smaller lattice parameters than InAs (InAs = 6.06 Å, ZnSe = 5.67 Å, and ZnS = 5.41 Å)[35,37,45,46] which typically leads to strain (and, consequently, interfacial defects) in the corresponding InAs@Zn(Se,S) core@shell QDs, often resulting in low PLQYs, with a maximum reported value of 13%.[37–40]

An effective way to enhance the emission of InAs@Zn(Se,S) QDs could be the use of InP as an interlayer, forming InAs@InP@ZnSe QDs, which have been proven to feature biocompatibility, biochemical stability, and low cytotoxicity.[37,41–44,46–51] InP can be beneficial for two reasons: 1) The InP lattice constant (5.87 Å) lies between that of InAs and ZnSe,[37,43] which may lead to the development of less strained InAs@InP@ZnSe QDs; 2) The bulk InP bandgap (1.34 eV) is larger than that of bulk InAs (0.35 eV) yet smaller than bulk ZnSe (2.70 eV),[37,52] potentially creating InAs@InP@ZnSe multi-shell heterostructures with a smooth energy barrier for the excitons originated in the core. This aspect is crucial, since in principle a smooth confinement potential can lead to a decrease in the rate of non-radiative Auger recombination.[27,53,54]

Despite the potential benefits of using InP as an interlayer, research on colloidal InAs@InP@shell QDs remains limited,[37,41–44,46–51] with a few studies reporting a wide range of PLQY values, from 23% in the case of InAs@InP@GaP@ZnSe QDs (PL at ≈1100 nm),[43] up to 76% for InAs@InP@ZnSe QDs (emission at ≈980 nm).[41,42] A common feature of all these studies is the redshift of the QDs absorption upon the growth of InP onto the InAs core, which has been attributed to the formation of a quasi type-II junction, despite the bulk band alignment of the core and shell materials pointing to a type-I heterojunction. The shift has thus been mostly attributed to isotropic delocalization of conduction band electrons in the InP shell, with holes being largely localized in the InAs core.[37,44,46,47,49,51] On the other hand, based on atomistic electronic structure calculations, Enright et al. recently proposed that holes may exhibit a facet-dependent delocalization into the InP shell through the anion-rich (-1-1-1) facets.[42]

Presently, there is a gap in the literature regarding an optical and structural study aiming at systematically increasing both the InP and Zn(Se,S) shell thicknesses. Such a study would provide insights into previously unanswered questions, such as:

1) **Band Alignment**. What is the actual band alignment between InAs and InP in InAs@InP core@shell QDs? The precise determination of the band alignment is complicated by the fact that, while the spectral absorption redshift (observed upon encapsulating InAs with InP) is consistent with charge separation in a quasi type-II junction, there is no clear consensus on how exactly the PL lifetime changes. Indeed, the PL lifetime in InAs QDs has not been studied in detail (with the only reported value being of 12 ns at room temperature[47]) and different PL lifetimes were reported for InAs@InP-based core@shell@shell QDs, ranging from 10 ns[55] to 11–17 ns,[42] 40 ns,[44] 60 ns,[48] and 70 ns.[46] Moreover, no studies have systematically investigated the variation in PL lifetime of InAs QDs and the resulting InA@InP QDs at cryogenic temperatures.
2) **Auger Recombination Rates**. Is the Auger recombination rate reduced when encapsulating InAs with InP and then ZnSe? Specifically, could InAs@InP-based QDs serve as optimal emitters for IR optoelectronic devices?

The open questions outlined above have motivated our current research work, where we first developed a colloidal synthesis route to prepare InAs@InP QDs with a fixed core size and a tunable shell thickness, ranging from ≈3 to 8 monolayers (MLs). This is the first time such heterostructures have been synthesized using safe, cost-effective, and environmentally friendly As and P precursors, specifically tris(dimethylamino)-arsine and tris(diethylamino)-phosphine (amino-As and amino-P, respectively). This approach contrasts sharply with the traditional use of pyrophoric, costly, and hazardous tris(trimethylsilyl)-arsine (TMS-As) and -phosphine (TMS-P) precursors in all previously documented InAs@InP-based core@shell QDs.

Our photophysical characterization revealed that the starting InAs QDs featured a low PLQY (≈2%), with a lifetime of 180 ns at 80 K. This is consistent with the PL stemming from the decay of excitons, wherein the holes are bound in shallow traps (associated with surface traps) resonant with the top of the valence band, as inferred from our density functional theory (DFT) calculations. The overgrowth of an InP shell led to InAs@InP QDs that: i) adopted a close to tetrapodal shape when increasing the InP shell thickness; and ii) featured a red-shifted absorption and PL spectra, and a higher PLQY (up to ≈13%). The latter was achieved only when post-treating the QDs with benzoyl fluoride to suppress surface defects.[56,57] The PL kinetics of these core@shell QDs was nearly single exponential, with a lifetime of 52 ns at 80 K (substantially faster than that of starting InAs QDs), consistent with the PL originating from free band edge excitons. Eventually, the overgrowth of a ZnSe shell resulted in InAs@InP@ZnSe QDs with atomically sharp interfaces and low lattice strain (lower than 1%). The optical analysis of such heterostructures revealed further suppressed non-radiative losses, resulting in a PLQY as high as 5≈55% and PL lifetimes close to those of the respective InAs@InP QDs. Overall, these results point to a band alignment where both carriers exhibit some degree of delocalization in the shell region and thus the InAs@InP QDs effectively function as "enlarged InAs QDs" rather than a quasi type-II system as previously hypothesized. Delocalization of both the charge carriers maintains an invariant carrier wavefunction overlap, which was evidenced by the similar Auger recombination rates in both the

**Table 1.** Composition of InAs, InAs@InP and InAs@InP@ZnSe QD samples measured by ICP-OES and corresponding size measured by TEM analyses.

| Sample | Elemental ratios | | | | Zn/Se | Size [nm] |
|---|---|---|---|---|---|---|
| | In/As | In/(As+P) | P/As | Zn/In | | |
| InAs core | 1.17 | 1.17 | / | 0.08 | / | 2.6 ± 0.2 |
| InAs@(1+2ML)InP | 3.07 | 1.06 | 1.91 | 0.06 | / | 3.7 ± 0.3 |
| InAs@(2+4ML)InP | 6.29 | 1.03 | 5.09 | 0.06 | / | 4.8 ± 0.3 |
| InAs@(3+5ML)InP | 9.91 | 1.06 | 8.36 | 0.05 | / | 5.9 ± 0.5 |
| InAs@(1+2ML)InP@(6ML)ZnSe | 4.89 | 2.00 | 1.44 | 3.94 | 1.07 | 8.5 ± 0.7 |
| InAs@(3+5ML)InP@(4ML)ZnSe | 9.22 | 1.39 | 5.64 | 1.03 | 0.84 | 7.6 ± 0.7 |

core-only, core@shell and core@shell@shell systems (in the order of ≈10 ps).

DFT analyses confirmed that in InAs@InP core@shell QDs charge carriers can delocalize into the shell. Specifically, electrons spread isotropically throughout the QD, while holes leak through the anion-rich facets into the shell, resulting in the experimentally observed redshift. This broadening of the wavefunction serves to augment the exciton size and increase oscillator strength, in line with the increase in PLQYs observed upon shelling InAs with InP.

## 2. Synthesis and Structural Characterization of InAs@InP core@shell and InAs@InP@ZnSe core@shell@shell QDs

For the synthesis of InAs QDs we adopted the procedure previously reported by our group, which utilizes $ZnCl_2$ as a crucial additive.[29,35] Specifically, $InCl_3$ and $ZnCl_2$ (maintaining a Zn:In precursors ratio of 10:1) were dissolved in oleylamine (OLAM). The temperature was raised to 240 °C followed by the swift injection of amino-As and the reducing agent (namely, alane N,N-dimethylethylamine). This step initiated the nucleation and subsequent growth of InAs QDs. The synthesis was halted after 20 min to prevent further growth, ensuring that the size of the QDs remained consistent across all the experiments. The overgrowth of the InP shell was performed at 180 °C and this involved adding a solution of $InCl_3$ in OLAM (0.2 M) and amino-P directly to the crude reaction mixture. The presence of $ZnCl_2$ in the reaction environment is critical, as it promotes the InP shell formation by activating the amino-P precursor.[38,40,58] Different shelling procedures were tested to preclude the homogeneous nucleation of InP QDs (see "*Optimization of the InP shell reaction*" section in Supporting Information). The optimized protocol consisted of a single injection of amino-P and $InCl_3$-OLAM precursors (with the amino-P/$InCl_3$ ratio fixed at 4, while the amino-P/amino-As ratio was 12:1) to achieve a shell thickness of ≈3 MLs, while multiple injections were required to increase the InP thickness up to ≈8 MLs (see the Experimental part for details).

The estimate of the shell thickness was based on a structural model featuring a 2.4 nm tetrahedral InAs core encased by an InP shell of variable thickness. We correlated the atomic ratios derived from this model with those obtained from elemental analyses, conducted using Inductively Coupled Plasma Optical Emission spectroscopy (ICP-OES) (**Table 1**, and Table S2, Supporting Information for further details). As will be demonstrated later in this section, the growth of InP onto InAs occurred first isotropically and then preferentially along the <-1-1-1> directions (Figure 2a). Taking this into account, the samples are named using the following notation: InAs@(x+yML)InP, where x stands for the InP MLs that are isotropically grown on the core, while y represents the shell MLs that are grown along the <-1-1-1> directions after the isotropic growth of x MLs. Low-resolution transmission electron microscope (TEM) images of InAs@InP core@shell QDs revealed that the size of the QDs expanded from 2.6 ± 0.2 nm (representing the InAs core) to 3.7 ± 0.3 nm (InAs@(1+2ML)InP), 4.8 ± 0.3 nm (InAs@(2+4ML)InP), and finally 5.9 ± 0.5 nm (InAs@(3+5ML)InP), as shown in **Figure 1** and Table 1. Additionally, there was no evidence of a secondary population of smaller nanocrystals (Figure 1b–d), which confirmed the effective suppression of InP homogeneous nucleation under our experimental conditions.

The XRD pattern of the InAs QDs corresponded to the cubic zinc-blende InAs phase (ICSD 98-002-4518) (Figure 1e). Notably, the positions of the XRD peaks shifted progressively toward higher two-theta angles as the thickness of the InP shell increased, getting closer to the positions expected for bulk InP (Figure 1f). The Raman spectrum of InAs QDs presented two prominent peaks, which are attributed to the transverse (TO) and the longitudinal (LO) optical modes of InAs at 212.8 and 228.8 $cm^{-1}$, respectively (Figure 1g, black curve, and Table S3, Supporting Information).[59,60] Following the growth of the InP shell, the Raman spectra of core@shell QDs revealed the emergence of TO and LO modes of InP at 316.7 and 342.4 $cm^{-1}$, respectively.[61] These modes became more pronounced as the thickness of the InP shell was increased (Figure 1g). Strain analysis, performed on the acquired Raman spectra,[62,63] indicated that the InAs core experiences a slight compressive strain, whereas the InP shell undergoes a slight tensile strain (Table S3, Supporting Information). This is in agreement with the larger lattice parameters of InAs compared to those of InP, further validating the successful growth of the InP shell on InAs QDs.

The increase in InP shell thickness resulted in a shape evolution toward a pronounced tetrapod-like structure for InAs@(2+4ML)InP and InAs@(3+5ML)InP QDs (**Figure 2**c,d). This shape evolution suggests a specific growth pattern: initially, the tetrahedral InAs cores were isotropically encapsulated within the InP shell, indicating no significant differences in kinetic growth among the InP facets. As the growth progressed, the (-1-1-1) facets grew preferentially compared to the (100) and (111)

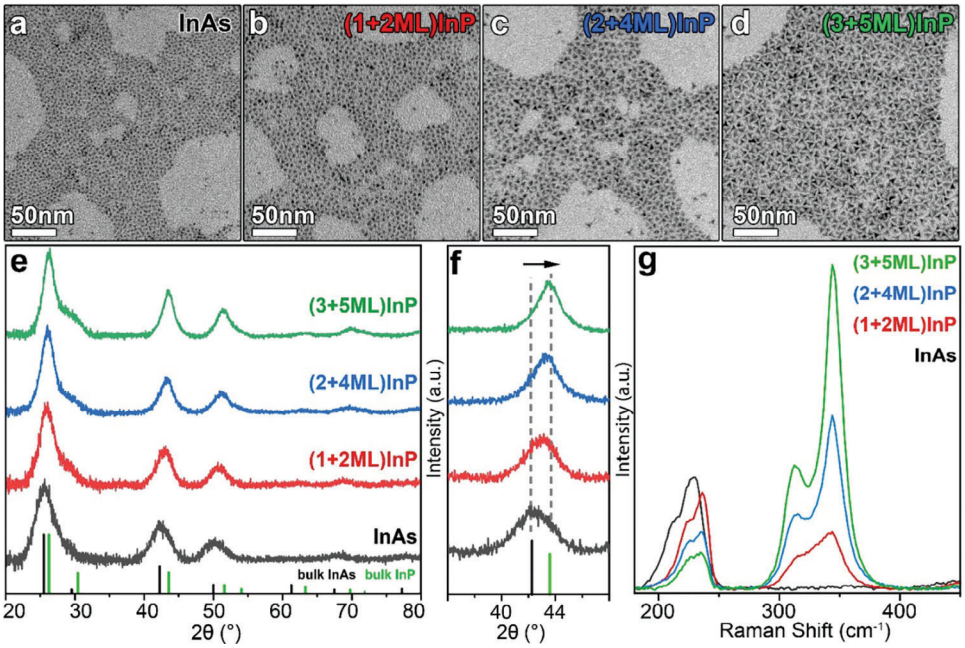


**Figure 1.** TEM images of InAs a) and InAs@InP QD samples with a variable InP shell thickness: b) InAs@(1+2ML)InP, c) InAs@(2+4ML)InP, and d) InAs@(3+5ML)InP. e) XRD patterns (with a magnified XRD range from 36° to 46° (f)) of the different QD samples together with the bulk reflections of InAs (ICSD 98-002-4518) and InP (ICSD 98-002-4517). g) Raman spectra of InAs and InAs@InP QDs, acquired using an excitation wavelength of 514 nm.

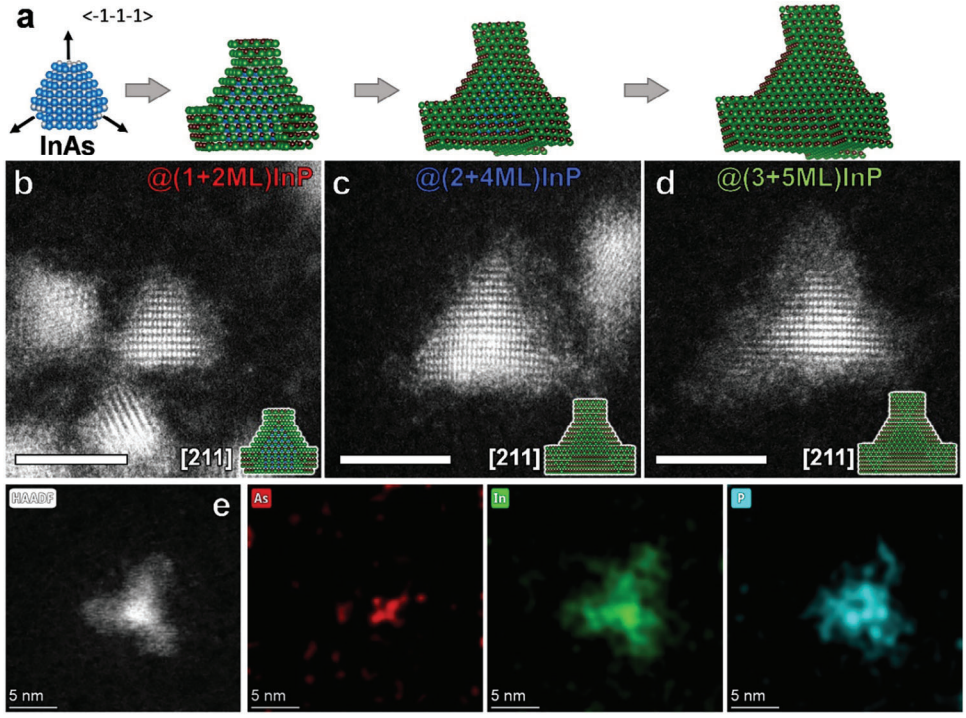


**Figure 2.** a) Structural models of InAs and InAs@InP QDs with a variable InP shell thickness. The <-1-1-1> crystallographic directions, along which InP shell preferentially grows, are indicated by arrows. The gray and dark magenta spheres represent As and P atoms, respectively. Blue and green spheres represent In atoms in the InAs and InP domains, respectively. b–d) HR-STEM-HAADF images of InAs@InP QDs with the shell thickness increasing from (b) 1+2 MLs, to (c) 2+4 MLs and (d) 3+5 MLs. In all the images, the QDs are observed along the [211] zone axis, and scale bars are 5 nm. The insets show the models projected along the [211] zone axis, aligned as the corresponding HR-STEM images. e) STEM-EDX elemental maps of a tetrapod-shaped InAs@(3+5ML)InP QD.

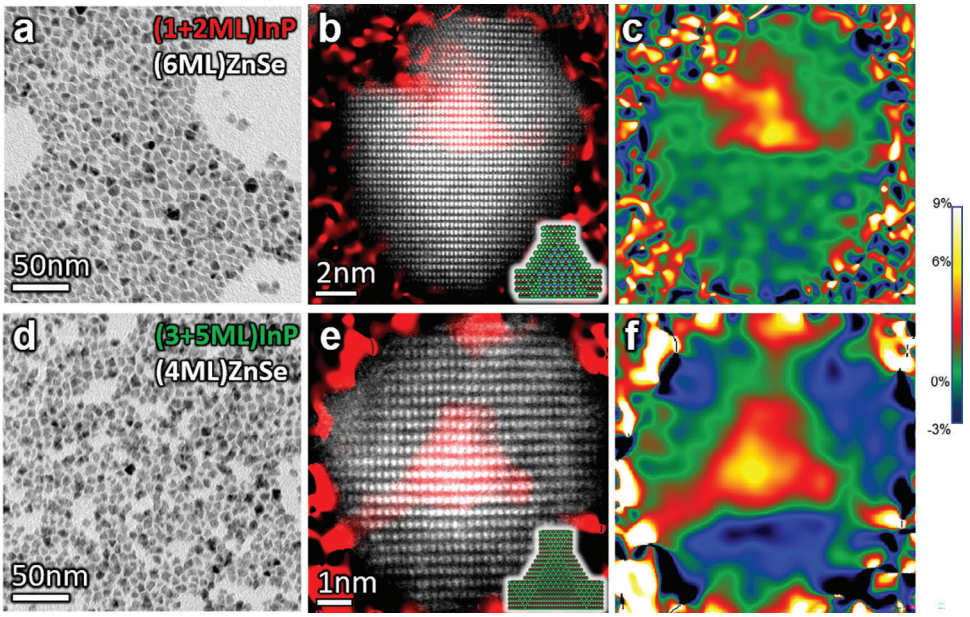


**Figure 3.** TEM images of a) InAs@(1+2ML)InP@(6ML)ZnSe and d) InAs@(3+5ML)InP@(4ML)ZnSe QDs. b,e) HR-STEM images of individual QDs oriented along the [211] zone axis, with aligned InAs@InP core@shell models in the inset. The corresponding results of GPA strain analysis are shown in (c,f) and as overlay in (b,e).

ones, directly contributing to the tetrapod-like shape (Figure S2, Supporting Information). The analysis of HR-STEM images supported this hypothesis, revealing the preferential growth of InP along the <-1-1-1> InAs crystallographic directions (Figure 2c,d). Despite the peculiar shape, all InAs@InP QDs are monocrystalline according to HR-STEM, which confirms the successful epitaxial growth of InP onto InAs. The growth of InP onto InAs was further proved by HR-STEM-EDX compositional analysis, in which the core@shell architecture is clearly visible (Figure 2e).

To tentatively explain the formation of the tetrapodal heterostructures, we compared our core@shell systems to those reported by Enright et al., who observed that the shell growth process was strongly anisotropic, leading to a non-uniform shell encapsulation that was thinner in the [111] direction, similar to our findings.[42] This suggests that the preferential growth of InP along certain crystallographic directions is not due to the specific reaction conditions employed in our work. Indeed, the InP shell growth of Enright et al. is based on TMS-P, which has much higher reactivity than amino-P, and uses oleic acid as a surfactant, whereas our scheme is based on oleylamine.

We therefore hypothesize that the preferential growth of InP along the <-1-1-1> directions is a way for the system to minimize interfacial strain (i.e., via stress relaxation), similar to what is commonly observed in epitaxy techniques. Indeed, it is well known that the growth of InAs onto InP by molecular beam epitaxy is dominated by elastic strain relaxation, which can be exploited to modulate the final shape of InAs self-organized nanostructures.[64,65]

To enhance the PL efficiency of InAs@InP QDs (see **Section 3**), we developed a synthesis strategy to encapsulate them within a ZnSe shell. The ZnSe shell growth was achieved in situ, by introducing Zn and Se precursors directly into the reaction flask containing the InAs@InP QDs, immediately after reaching the desired InP shell thickness. Specifically, after quenching the InP growth, we added tri-n-octylphosphine (TOP), a $ZnCl_2$-OLAM (0.8 M) solution, and a TOP-Se (2 M) solution, and the resulting mixture was then heated up to 340 °C (see "*Optimization of the ZnSe shell reaction*" in the Supporting Information). We focused on two representative InP shell thicknesses, (1+2) and (3+5) MLs (namely the thinnest and thickest of our set), and we optimized the ZnSe shell thickness by monitoring the PLQY as a function of ZnSe shell growth time (Figures S3 and S4, Supporting Information). Similar to the InAs@InP case, here too the ZnSe shell thickness was estimated using a structural model consisting of a 2.4 nm tetrahedral InAs core encased by a (1+2ML) or (3+5ML) InP shell, with a variable ZnSe thickness (Figure S2, Supporting Information). Atomic ratios from this model were then correlated with those obtained from ICP elemental analyses (see Table 1, and Tables S5 and S6, Supporting Information for further details). The optimized ZnSe shell thicknesses obtained for InAs@(1+2ML)InP and InAs@(3+5ML)InP QD samples were 6 and 4 MLs, respectively (Table S2, Supporting Information). TEM images of core@shell@shell QDs indicated that the size of the InAs@(1+2ML)InP QDs increased from 3.7 ± 0.3 to 8.5 ± 0.7 nm and that of InAs@(3+5ML)InP QDs expanded from 5.9 ± 0.5 to 7.6 ± 0.7 nm (**Figure 3**a,b and Table 1). In both cases the ZnSe shell growth led to shifts of the XRD peaks toward higher two theta angles, in agreement with the smaller lattice parameters of ZnSe compared to those of InAs and InP (Figure S5, Supporting Information).

The ICP analyses of the whole series of samples revealed that: i) The InP shell underwent an etching process during the ZnSe shell growth, which resulted in a decrease of the P/As atomic ratio. In the InAs@(1+2ML)InP case, this etching was less pronounced and led to a decrease of the P/As ratio from ≈1.9 to ≈1.4 (Table 1; and Table S5, Supporting Information). On the

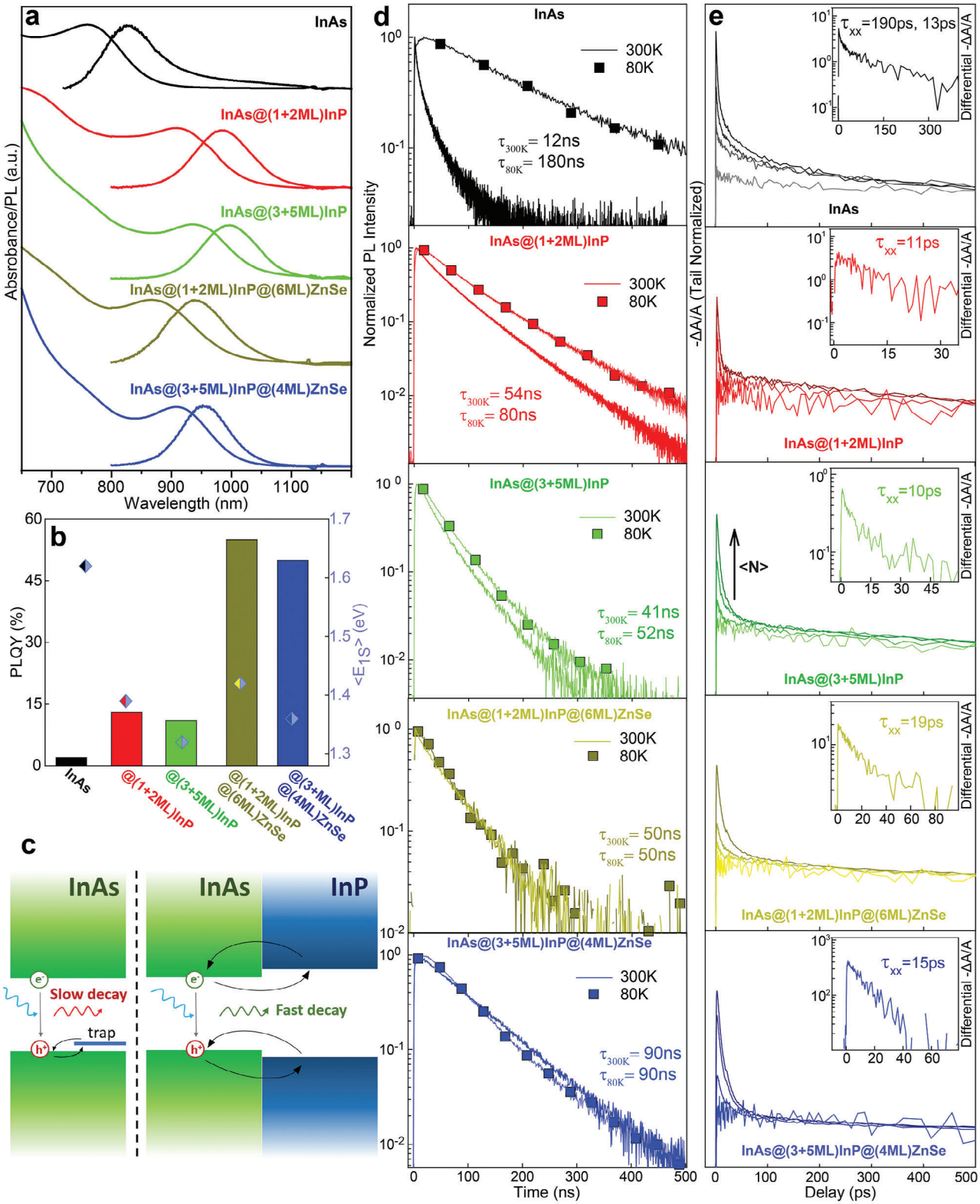


**Figure 4.** a) Absorption and PL spectra of InAs, InAs@(1+2ML)InP, InAs@(3+5ML)InP, InAs@(1+2ML)InP@(6ML)ZnSe and InAs@(3+5ML)InP@(4ML)ZnSe QDs in toluene, and b) corresponding PLQY and band edge energy (<$E_{1S}$>). c) Schematic representation of photophysics of core only and core@shell QDs. d) PL time decay profiles at room temperature and 80 K, and e) TA decay profiles of the QD samples at varying excitation fluence in order to keep the average number of excitons per QDs (⟨N⟩) in the range of ≈0.05 to ≈2.5 (inset shows the differential TA curves representing biexciton decay profiles of the corresponding QDs).

**Table 2.** Absorbance and PL peak position, PLQY, PL lifetime ($\tau_X$) at 300 and 80 K and biexciton lifetime ($\tau_{XX}$) of InAs, InAs@InP and InAs@InP@ZnSe QD samples.

| Sample | Abs peak [nm] | PL peak [nm] | PLQY [%] | $\tau_X$ 300 K [ns] | $\tau_X$ 80 K [ns] | $\tau_{XX}$ [ps] |
|---|---|---|---|---|---|---|
| InAs core | 760 | 829 | 2 | 12 | 180 | 13 |
| InAs@(1+2ML)InP | 908 | 984 | 13 | 54 | 80 | 11 |
| InAs@(3+5ML)InP | 935 | 997 | 11 | 41 | 52 | 10 |
| InAs@(1+2ML)InP@(6ML)ZnSe | 866 | 939 | 55 | 50 | 50 | 19 |
| InAs@(3+5ML)InP@(4ML)ZnSe | 909 | 953 | 50 | 90 | 90 | 15 |

other hand, in the InAs@(3+5ML)InP case such etching was observed to be more significant, with the P/As ratio decreasing from ≈8.4 to ≈5.6 (Table 1; and Table S6, Supporting Information). Notably, while the InP etching in the InAs@(1+2ML)InP case was observed to occur mostly at the early stages of the ZnSe shell growth, in the InAs@(3+5ML)InP case such etching occurred during most of the ZnSe shell growth. Similar values were obtained by X-ray photoelectron spectroscopy (XPS) (Table S7, Supporting Information). ii) In was incorporated into the ZnSe shell, particularly in the first shell layer. This was particularly evident when growing ZnSe onto InAs@(1+2ML)InP QDs where, despite the slight etching of the InP shell, we observed an increase in the In/As ratio from 3.1 (3.2 via XPS) in InAs@(1+2ML)InP to 4.9 (7.0 via XPS) in InAs@(1+2ML)InP@(6ML)ZnSe samples (Table 1; and Tables S5 and S7, Supporting Information). The majority of the observed increase occurred during the initial stages of ZnSe shell growth, as demonstrated by the sample where the ZnSe shell grew for 15 min onto InAs@(1+2ML)InP QDs and resulting in an In/As ratio of 4.9 (6.1 via XPS) (Tables S5 and S7, Supporting Information). This suggested that the "extra In" was mainly localized in the first layer close to the InP/ZnSe interface. These observations are compatible with the formation of an In-Zn-Se interlayer, in analogy with recent observations on InAs@ZnSe and InP@ZnSe QD systems.[29,35,66]

HR-STEM images of these samples revealed that such heterostructures were single crystals (Figure 3b,e). Geometric Phase analysis (GPA) of InAs@(1+2ML)InP@(6ML)ZnSe and InAs@(3+5ML)InP@(4ML)ZnSe QDs indicated the absence of lattice strain in both cases (Figure 3c,f). Specifically, the local difference in lattice parameters (within one atomic plane) between the InAs core, InP and ZnSe shells corresponded to the difference in the bulk lattice parameters of these materials. Moreover, the HR-STEM analysis demonstrated that the starting InAs@InP QDs roughly preserved their original shape upon ZnSe shell growth: the InAs@(1+2ML)InP "core" in InAs@(1+2ML)InP@(6ML)ZnSe QDs exhibited a nearly-tetrahedral shape (Figure 3b), prompting subtle etching on the (-1-1-1)-facets. Conversely, the InAs@(3+5ML)InP "core" in InAs@(3+5ML)InP@(4ML)ZnSe QDs featured more pronounced etching on the same facets while maintaining a tetrapod shape (Figure 3e). This etching process along the <-1-1-$_{XX}$1>-directions in both systems would explain the different decrease of P/As and In/As ratios, indicating a preferential loss of P over In, implying more significant etching on anion-rich facets such as the (-1-1-1) ones (Figure S2 and Table S2, Supporting Information for further details).

## 3. Optical Characterization of InAs, InAs@InP, and InAs@InP@ZnSe QDs

**Figure** 4a shows the absorption spectra of InAs QDs, InAs@InP core@shell QD samples with the thinnest and thickest InP shell (namely InAs@(1+2ML)InP and InAs@(3+5ML)InP and the corresponding InAs@InP@ZnSe QDs (i.e., InAs@(1+2ML)InP@(6ML)ZnSe and InAs@(3+5ML)InP@(4ML)ZnSe). InP shelling resulted in a red shift of the lowest energy excitonic transition in the absorption spectra (**Table** 2), consistent with the delocalization of the charge carriers in the InP shell, effectively increasing the exciton size, as confirmed by our DFT calculations (see Section 4). Further shelling of these InAs@InP QDs with ZnSe resulted in slightly blue-shifted spectral features (Table 2). This is in line with the etching of part of the InP shell observed when growing the ZnSe shell (see Section 2). Further insights into the photophysics of these systems were gained through PL and PLQY analysis and time-resolved PL measurements (Table 2). InAs QDs featured a very low PLQY ≈2% (Figure 4b) and a fast, multi-exponential decay kinetics with an effective lifetime of 12 ns (defined as the time after which the PL intensity had dropped by a factor *e*, Figure 4d) in agreement with what reported by Wijaya et al.[47] Cooling the InAs QDs to 80 K slowed down the decay rate by 15-fold, resulting in a largely single-exponential kinetics featuring a lifetime as long as 180 ns. This result is consistent with the predicted existence of shallow trap states in resonance with the valence band maximum of InAs QDs, as proposed by our DFT calculations (vide infra), resulting in slow radiative decay kinetics. At room temperature, however, the InAs QDs exhibited limited surface passivation, causing rapid surface trapping of charge carriers, which accounts for the observed fast decay and low PLQY.

Upon the growth of the InP shell, the resulting core@shell QDs featured an extremely poor PL, in agreement with previous reports.[41,44,55] It is important to note that, in some studies, the emission from InAs@InP QDs has been clearly observed.[43,44,46–49] A common feature in these studies was the use of a Zn precursor combined with tris(trimethylsilyl)-phosphine (TMS-P) for the growth of the InP shell. We hypothesize that such PL emerges as a consequence of the presence of Zn which, under TMS-P based synthesis schemes, is known not only to facilitate the formation of In(Zn)P, but also to provide an efficient surface passivation (i.e., leading to a Zn-carboxylate covered surface).[43,55] To improve the PL efficiency of our core@shell QDs, we exposed them to a water-free HF treatment (based on

the use of benzoyl fluoride, see the Experimental Section for details), which is known to efficiently remove non-radiative traps from the surface of amino-P based InP QDs.[56,57] This resulted in InAs@(1+2ML)InP and InAs@(3+5ML)InP QDs with PLQY values of 13% and 11%, with room temperature lifetimes of 54 and 41 ns, respectively (Figure 4b,d). Cooling these QDs to 80 K caused a slight decrease in their decay kinetics (ca. 1.3-fold lower, with lifetimes being 80 and 52 ns, respectively). The faster radiative decay of InAs@InP with respect to InAs QDs indicated the effective removal of resonant trap states present on the surface of the initial InAs QDs. This resulted in a band-edge free-exciton photophysics with nearly complete overlap of electron and hole wavefunctions.

Finally, further shelling the InAs@InP QDs with ZnSe yielded core@shell@shell systems with considerably enhanced PLQY (up to ≈55%, see Figure 4b and Table 2) and good stability in air, with ≈80% of the PL intensity retained after 14 days of air exposure (Figures S3 and S4, Supporting Information). Interestingly, the PL lifetimes of these multi-shell QDs were similar to those of the respective InAs@InP QDs and remained invariant with decreasing temperature (Figure 4d). This indicated that the reduced PLQY in InAs@InP QDs, as well as the residual losses in the multi-shell QDs, are likely due to ultrafast surface trapping that depletes the band edges without affecting the PL kinetics. Indeed, the fact that the PLQY increases with decreasing temperature at constant PL lifetime points exactly in this direction, where "slow" quenching channels are negligible compared to the thermal suppression of trapping happening within our time resolution, which typically requires overcoming a potential barrier.

To investigate the multi-exciton dynamics, transient absorption spectroscopic (TA) measurements were carried out by varying the pump fluence according to the desired value of the average number of excitons, ⟨N⟩, per QD. All systems showed TA dynamics consistent with their single exciton PL lifetime at low ⟨N⟩-values, and a sub-nanosecond component arising and intensifying with increasing excitation fluence, due to growing multi-exciton population (Figure 4e). Subtraction of the tail normalized single exciton decay from TA profiles at higher exciton population enabled us to extract the biexciton (XX) kinetics, as reported in the insets of Figure 4e and Table 2. The InAs QDs showed biexponential biexciton dynamics with a slow 190 ps component featuring the contribution from resonant surface traps with reduced carrier overlap and a minor 13 ps component from the band edge excitons. Shelling with InP led to a single exponential biexciton kinetics ($\tau_{XX}$ = 11 ps) due to effective removal of trap states. Further encapsulation within ZnSe led to minor slowing down of the XX decay ($\tau_{XX}$ = 19 ps) consistent with the substantial invariance of the spectral profile. In all the QD systems, the biexciton quantum yield was calculated to be less than 0.1%, indicating that neither InP nor ZnSe shells lead to any significant suppression of Auger recombination losses. This further supports the fact that: 1) in InAs@InP QDs both carriers can delocalize in the shell, with no measurable effect on the wavefunction overlap; 2) the final overgrowth of a ZnSe shell results in a type-I band alignment between this shell and the "InAs@InP" core, thereby not significantly altering the carriers' overlap.

Overall, the spectroscopic investigation suggests that InP and ZnSe shelling is a valuable strategy to enhance the PLQY of InAs QDs and concomitantly accelerate the emission kinetics by suppressing surface defects. The PLQY values reported here are indeed close to those achieved for amino-As InAs@ZnSe QDs in recent reports from our group (i.e., 70%).[29,35] However, such strategy is essentially inconsequential for the multiexciton photophysics that remains largely dominated by nonradiative Auger decay.

## 4. DFT Calculations/ First Principles Simulations

To rationalize the optical properties (see Section 3) of InAs@InP core-shell QDs, we prepared two different model types: i) cuboctahedral QD models, with the (100)- and (111)-facets exceeding the size of their (-1-1-1)-facets to maintain the systems charge-balanced (as depicted in **Figure 5**a for models 1–3); ii) tetrapod-like shaped QD models with extended arms along the (-1-1-1)-facets (see models tp-4 to tp-6 in Figure 5a). For simplicity, the tetrapod-like models were based on a core size of 1.2 nm, although the results can be extrapolated to larger systems (Figure S7, Supporting Information). The shape evolution of our models is inspired by the QDs synthesized in this work (Figure 2b,c), and follows the same surface criteria outlined in the work of Llusar et al.[67]

Our DFT calculations revealed a redshift in absorption/emission as the number of InP MLs increases for the cuboctahedral models. This shift was less pronounced when the core size was larger (Figure 5a). Interestingly, while a significant redshift of ≈1 eV is observed when moving from 1.2 nm InAs QD to cuboctahedral InAs@(5ML)InP (model **1** and **6** in Figure 5a, respectively), a notable reduction in the red shift was observed when transitioning from model **1** to tetrapod-like InAs@(5ML)InP (model **tp-6** in Figure 5a). This red shift saturation phenomenon correlates directly with the MLs growth onto the (-1-1-1)-facets, suggesting that tetrapod-like InAs@InP QDs are less sensitive to quantum confinement along these facets and in line with the experimental observation of a small redshift when going from InAs@(1+2ML)InP to InAs@(3+5ML)InP (Figure 4a). If a pure InAs@InP cuboctahedron had formed, a marked redshift would indeed be observed. However, this confinement seems to affect more strikingly the HOMO states, as LUMO states tend to delocalize isotropically throughout the entire QD, regardless of shape, as shown in Figure 5c-(iv–vi).

To elucidate the variations in optical features observed when growing the InP shell onto InAs cores, we computed the oscillator strengths for the lowest energy transitions from model **1** to model **tp-6**. Our analysis also included an InAs core with surface defects (model **0** in Figure 5) to match the observation of a negligible PLQY for pure core InAs QDs. This defective QD was obtained by randomly detaching various $InCl_3$ Z-type ligands from the surface. Although, this system shows a non-zero HOMO – LUMO gap (Figure 5b-i) and, counterintuitively, some degree of delocalization due to its small size (Figure 5c-i), it practically yields a null oscillator strength, thus confirming a poor PLQY (Figure 5d). To avoid ambiguity, we conducted an Inverse Participation Ratio (IPR) analysis to determine the degree of localization of the MOs shown in Figure 5b-i (Figure S8, Supporting Information). The IPR analysis revealed that model **0**, due to its small size, exhibits several trap states within both the conduction and valence bands, with a pronounced accumulation of traps

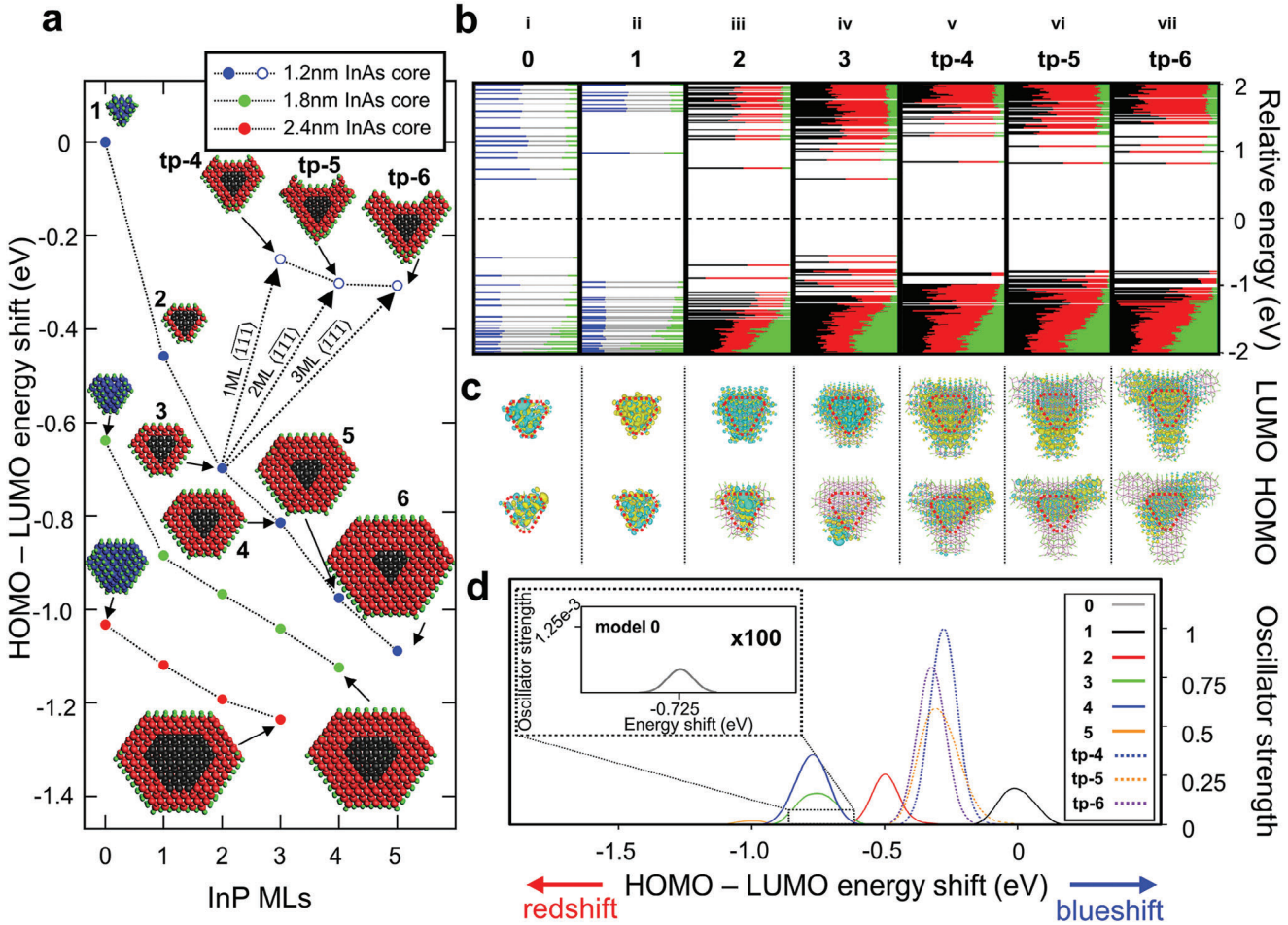


**Figure 5.** a) Red shift associated with the number of InP shell MLs (crystalline domain in red color) grown on InAs core QDs (blue crystals) of varying sizes. Blue, green, and red filled circles stand for QDs made of InAs core sizes of 1.2, 1.8, and 2.4 nm, respectively. The blue empty circles represent the tetrapod-shaped InAs@InP QDs with an InAs core size of 1.2 nm. The energy origin is set by the core-only InAs model **1**. b) Density of States (DOS). Each horizontal line corresponds to a molecular orbital (MO). The length of the colored line segments for **0** and **1** depicts the contribution of each element to a MO; blue, grey and green line segments represent In, As, and Cl atoms, respectively. Additionally, from model **2** to **tetrapodal (tp)−6**, the contribution of core, shell, and Cl atoms to an MO is illustrated by black, red, and green line segments, respectively. Levels below the dashed line are valence band states; levels above are conduction band states. c) MO plots of the HOMO and LUMO for each system. Red dotted lines represent the space occupied by the InAs core. d) Oscillator strengths of the lowest energy transitions of each system. Energies are adjusted in relation to the core-only InAs model **1**. The inset depicts a 100x-zoomed-in view of the oscillator strength for the defective InAs model.

at the top of the valence band (Figure S8a, Supporting Information). This is even more significant in a poorly-passivated 2.4 nm InAs QD, where shallow trap states primarily form at the top of the valence band (Figure S8b, Supporting Information). This can also be intuitively explained by considering that InAs QDs are terminated by the <111>-, <100>-, and <-1-1-1>-facets. The first two facets are In-rich and efficiently accept ligands, thereby saturating their dangling bonds. In contrast, the <-1-1-1>-facets, which are As-rich, cannot be passivated as efficiently. This leaves As atoms with dangling bonds exposed at the surface. Therefore, in this type of system, it is more likely to feature hole traps (due to the dangling bonds of As atoms) instead of electron traps. These results would explain the slow radiative decay kinetics of InAs core QDs (Figure 4c), which can be attributed to the presence of shallow trap states resonating with the valence band maximum (as discussed in Section 3).

After removing these defects, as represented by the DOS of model **1**, the HOMO – LUMO gap energy increased considerably (Figure 5b-ii), showing a 200-fold increase in oscillator strength compared to its defective counterpart (Figure 5d). Then, upon systematically coating the undefective InAs core with up to 2 MLs of InP, resulting in model **2** and **3**, the electron and hole charge densities, which were evenly distributed throughout the entire QD for model **2** (Figure 5c-iii), began to exhibit differences in terms of delocalization. In agreement with the work of Enright et al.,[42] our models indicated that while the electron charge density remains delocalized isotropically across the QD, the hole charge density begins to show seemingly some preference for leaking through the (-1-1-1)-facets (Figure 5c-iv). Following this, we observed a low oscillator strength (Figure 5d) for the defective InAs core, which simulates the first stages of the InAs QD growth. Subsequently, we assumed a surface-corrected InAs QD,

where the defects are removed, and the epitaxial growth of the InP would be optimal. This situation leads to an increase in the oscillator strength. Noticeably, when growing the InP shell along the <-1-1-1>-directions, thus forming the tetrapod-like core-shell QDs (models **tp-4** to **tp-6**), we observed that the electron charge density was efficiently delocalized within the whole QD, while the hole charge density showed a clear tendency to leak through (-1-1-1)-facets (Figure 5c-(v–vii)). This leakage seems to be less prominent in larger QDs, and this may explain why the oscillator strength is slightly weaker in model **tp-6** than in model **tp-4**, in line with the slightly lower PLQY of InAs@(3+5ML)InP with respect to that of InAs@(1+2ML) QDs.

Overall, our DFT calculations demonstrate the significant role of structure and surface passivation on the optical properties of InAs@InP core@shell QDs. The presence of an InP shell suppresses surface trap states of the InAs core (mostly localized close to the top of the valence band), thus improving the overall PLQY. On the other hand, the InP shell cannot prevent delocalization of the electron and hole wavefunctions onto the InP shell. The electron charge density indeed uniformly disperses across the whole core@shell quantum dot, whereas hole charge density delocalization is less pronounced, showing facet-dependent leakage due to a weakened quantum confinement in the (-1-1-1)-facets. Overall, this effect impedes the formation of either type-I or quasi type-II heterostructures, as one would be led to infer from bulk energy diagrams.

## 5. Conclusion

We have developed a colloidal synthesis approach to prepare InAs@InP core@shell QDs using tris(dimethylamino)-arsine and tris(diethylamino)-phosphine, enabling a tunable shell thickness. We observed that InP grew epitaxially onto InAs QDs preferentially along the <-1-1-≈1> directions, resulting in core@shell QDs with a tetrapodal shape. Optically, the InP shelling onto InAs induced a red-shift in absorption and PL spectra, along with an increase in PLQY (from 2% to ≈13%). Post-treating the InAs@InP QDs with benzoyl fluoride was essential to achieve this enhancement by suppressing surface defects. The PL kinetics of these InAs@InP QDs exhibited single-exponential behavior with a lifetime of 52 ns at 80 K, indicating PL generation by free band-edge excitons. Notably, the starting InAs QDs featured a long PL lifetime (180 ns) due to the presence of shallow trap states resonant with the top of the valence band, as revealed by our DFT calculations. To further enhance the optical performance, we epitaxially grew a ZnSe shell layer in situ on the InAs@InP samples. The resulting InAs@InP@ZnSe QDs exhibited a PLQY as high as ≈55%, good stability in air (≈80% of the PL intensity retained after 14 days of air exposure) and PL lifetimes similar to those of the corresponding InAs@InP QDs.

Overall, our spectroscopic analyses indicated that in InAs@InP QDs both carriers exhibit some degree of delocalization in the InP shell region, causing the systems to behave more like "enlarged InAs QDs" rather than type-I or quasi type-II heterostructures, as previously assumed. DFT calculations suggested that electrons could delocalize throughout the entire InP shell, while holes could preferentially tunnel into the shell along the <-1-1-1> directions. Consistent with this, our transient absorption spectra, recorded as a function of excitation fluence, revealed fast Auger recombination rates in all structures (on the order of ≈10 ps). Consequently, our findings indicate that on one hand, amino-As and amino-P based InAs@InP@ZnSe QDs can be synthesized with high PL efficiency, thus showing promise as NIR emitters. On the other hand, to further enhance the optical properties of InAs-based QDs in terms of Auger recombination rates, exploration of different combinations of shell materials beyond those investigated here should be pursued.

## 6. Experimental Section

*Chemicals*: Indium(III) chloride ($InCl_3$, 99.999%, Sigma-Aldrich), zinc(II) chloride ($ZnCl_2$, 99.999%, Sigma-Aldrich), tris(dimethylamino)arsine (amino-As, 99%, Strem), alane N,N-dimethylethylamine complex solution (DMEA-$AlH_3$, 0.5 M solution in toluene, Sigma-Aldrich), tris(diethylamino)phosphine (amino-P, 97%, Sigma-Aldrich), selenium powder (Se, 99.99%, Strem), benzoyl fluoride (98%, TCI), triethyloxonium tetrafluoroborate ($Et_3OBF_4$, 97%, Sigma-Aldrich), oleylamine (OLAM, 98%, Sigma-Aldrich), tri-n-octylphosphine (TOP, 97%, Strem), mesitylene (97%, Sigma-Aldrich), tributylphosphine (TBP, 97%, Sigma-Aldrich), octylamine (99%, ThermoFisher) toluene (anhydrous, 99.8%, Sigma-Aldrich), ethanol (anhydrous, 99.8%, Sigma-Aldrich), hexane (anhydrous, 95%, Sigma-Aldrich), and N,N-dimethylformamide (DMF, anhydrous, 99.8%, Sigma-Aldrich). All the chemicals were used without further purification.

*Preparation of the As Precursor*: In a glovebox filled with $N_2$, 0.2 mmol of amino-As (37 µL) were mixed with 0.5 mL of degassed OLAM at 40 °C for 5 min until no further bubbles evolved.

*Preparation of $InCl_3$-OLAM (0.2 M) Precursor*: In an $N_2$-filled glovebox, 2 mmol of $InCl_3$ was dissolved in 10 mL of OLAM in a 20 mL glass vial by heating the mixture to 250 °C under stirring for 30 min. The solution was then cooled down to room temperature.

*Preparation of $ZnCl_2$-OLAM (0.8 M) Precursor*: In a $N_2$ filled glovebox, 6 mmol of $ZnCl_2$ was dissolved in 7.5 mL of OLAM in a 20 mL glass vial by heating the mixture to 250 °C under constant stirring for 30 min. $ZnCl_2$ precipitates at room temperature, therefore the solution must be heated up to 150 °C before use.

*Preparation of the TOP-Se (2 M) Precursor*: In a $N_2$ filled glovebox, 20 mmol of Se powder was mixed with 10 mL of TOP in a 20 mL glass vial and heated at 250 °C under stirring for 30 min. The resulting solution was cooled down to room temperature.

*Synthesis of InAs QDs*: InAs QDs were synthesized following the procedure reported in the previous works.[29,35,68] In a typical synthesis, 0.2 mmol of $InCl_3$, 2 mmol of $ZnCl_2$, and 5 mL of OLAM were loaded into a 100 mL three-necked flask under inert atmosphere, and the mixture was degassed at 120 °C under vacuum for 1.5 h. The resulting solution was heated to 240 °C under nitrogen, and the amino-As precursor was injected into the flask, quickly followed by the injection of 1.2 mL of the DMEA-$AlH_3$ toluene solution (0.5 M). The reaction was quenched after 20 min by removing the heating mantle and allowing it to naturally cool down to room temperature. To ensure that the size of the resulting InAs QDs remained constant throughout all the experiments reported in this work, it was verified each time that the excitonic absorption peak was consistently positioned at ≈760 nm. The QDs were cleaned by the addition of 15 mL of ethanol and precipitated by centrifugation at 4000 rpm for 5 min. The supernatant was discarded, and the precipitate was dispersed in 3 mL of toluene, followed by precipitation via the addition of 9 mL of ethanol and centrifugation at 4000 rpm for 5 min. The purification procedure was repeated for two times. The collected InAs QDs were dispersed in toluene for further characterization. All the purification steps were performed under a $N_2$ atmosphere.

*Synthesis of InAs@InP core@shell QDs*: After quenching the InAs QDs reaction by removing the heating mantle, the temperature naturally cooled down to 140 °C, and then the desired amount of $InCl_3$-OLAM (0.2 M) (ranging from 3 to 6 mL) was injected into the reaction flask followed by the addition of the desired amount of the amino-P precursor (ranging from

**Table 3.** Amounts of amino-P and $InCl_3$-OLAM (0.2 M) precursors employed in the different injections in order to produce InAs@InP with the shell thickness tunable from 1.5 to 4ML.

| Samples | 1st cycle | | 2nd cycle | | 3rd cycle | | 4th cycle | | 5th cycle | |
|---|---|---|---|---|---|---|---|---|---|---|
| | Amino-P | $InCl_3$-OLAM | Amino-P | $InCl_3$-OLAM | Amino-P | $InCl_3$-OLAM | Amino-P | $InCl_3$-OLAM | Amino-P | $InCl_3$-OLAM |
| InAs@(1+2ML)InP | 2.4 mmol | 3 mL | | | | | | | | |
| InAs@(2+4ML)InP | 2.4 mmol | 6 mL | 1.2 mmol | / | 1.2 mmol | / | | | | |
| InAs@(3+5ML)InP | 2.4 mmol | 6 mL | 1.2 mmol | / | 1.2 mmol | / | 1.2 mmol | 3 mL | 1.2 mmol | / |

1.2 to 2.4 mmol, see **Table 3** below for details). The resulting mixture was heated up to 180 °C for 60 min and then cooled down to room temperature to quench the InP growth. This procedure was repeated multiple times (up to 5 times) to increase the shell thickness from 3 to 8ML. In each cycle: i) the desired amounts of amino-P and $InCl_3$-OLAM (as shown in Table 3) were added to the crude reaction solution at 140 °C; ii) the resulting mixture was heated to 180 °C for 60 min; iii) the reaction was quenched by removing the flask from the heating mantle and allowed to cool down to room temperature. The resulting InAs@InP core@shell QDs were cleaned by adding three volumes of ethanol to the raw reaction mixture, and then precipitated by centrifugation at 2000 rpm for 5 min. The supernatant was discarded, and the precipitate was dispersed in 3 mL of toluene, followed by precipitation with the addition of 9 mL of ethanol, and then the mixture was centrifuged at 4000 rpm for 5 min. The above purification was repeated twice. The collected InAs@InP core@shell QDs were dispersed in toluene for further characterization. All purification steps were performed under a nitrogen atmosphere.

*Synthesis of InAs@InP@ZnSe core@shell@shell QDs*: After quenching the growth of the InP shell at the desired thickness by removing the heating mantle, the temperature of the reaction mixture naturally cooled down to 90 °C. Subsequently, 7.5 mL of the $ZnCl_2$-OLAM (0.8 M) precursor and a mixture consisting of 4 mL of TOP-Se (2 M) and 3 mL of TOP (see the corresponding section "optimization of the ZnSe shell thickness" in the Supporting Information) were injected into the crude reaction mixture. The resulting mixture was heated up to 340 °C and kept at that temperature for the desired reaction time (i.e, the InAs@(1+2ML)InP@ZnSe sample for 40 min and the InAs@(3+5ML)InP@ZnSe sample for 90 min, see the Supporting Information for further details). The reaction was quenched by removing the flask from the heating mantle and cooling it down to room temperature. The raw InAs@InP@ZnSe core@shell@shell QDs were cleaned by adding two volumes of ethanol to the raw reaction mixture, and then precipitated by centrifugation at 2000 rpm for 5 min. The supernatant was discarded, and the precipitate was dispersed in 5 mL of toluene, followed by precipitation with the addition of 10 mL of ethanol, and then the mixture was centrifuged at 2000 rpm for 5 min. This purification process was repeated twice. The final InAs@InP@ZnSe core@shell@shell QDs were dispersed in toluene for further characterization. All purification steps were performed under a $N_2$ atmosphere.

*Treatment of InAs@InP core@shell QDs with Benzoyl Fluoride*: The treatment protocol using benzoyl fluoride for InAs@InP QDs was performed according to the procedure reported by Yadav et al.[57] All treatment processes were performed inside the $N_2$-filled glovebox at room temperature. InAs@(1+2ML)InP QDs (3.5 mg) or 8.5 mg of InAs@(3+5ML)InP QDs were dispersed in 6 mL of mesitylene, followed by the addition of a 210 µL of $ZnCl_2$-TBP solution (0.64 M, obtained by dissolving 18.3 mg of $ZnCl_2$ in 210 µL of TBP for 60 min at room temperature) and a mixture of 110 µL of octylamine and 940 µL of mesitylene. Subsequently, a mixture of 72 µL of octylamine and 978 µL of mesitylene was added to the previous mixtures drop by drop. After allowing the treatment of InAs@InP QD samples running for 20 min, the resulting products were washed by adding 40 mL of ethanol and then centrifuging at 6000 rpm for 10 min. The precipitate was collected and dispersed in toluene for further characterization. The final QDs were stored in the $N_2$-filled glovebox.

*Ligand Stripping Procedure*: A ligand stripping procedure was employed to prepare QDs for high-resolution transmission electron microscopy (to avoid any contamination from organic ligands), and it was performed by following the procedure reported by Rosen et al.[69] In a $N_2$-filled glovebox, 0.5 mL of a QDs dispersion (in toluene) was added to 1 mL of hexane in a glass vial, and then 1 mL of a solution of $Et_3OBF_4$ in DMF (100 mM) was added into the vial. After shaking the vial for several seconds, the QDs were transferred from the hexane into the DMF phase. The QDs dispersed in DMF were precipitated by the addition of toluene followed by centrifugation at 4000 rpm for 5 min. To remove residual organic ligands, the washing procedure was repeated twice and the resulting QDs were dispersed in DMF.

*X-Ray Diffraction (XRD)*: XRD patterns were acquired with a PANanalytical Empyrean X-ray diffractometer equipped with a 1.8 kW Cu K$\alpha$ ceramic X-ray tube and a PIXcel3D 2×2 area detector, operating at 45 kV and 40 mA. Specimens for XRD measurements were prepared by dropping a concentrated QDs solution onto a silicon zero-diffraction single crystal substrate. The diffraction patterns were recorded under ambient conditions using a parallel beam geometry and the symmetric reflection mode. XRD data analysis was performed by using the HighScore 4.1 software from PANalytical.

*Transmission Electron Microscopy (TEM)*: Diluted QDs dispersions were drop-cast onto copper TEM grids with an ultrathin carbon film. Low-resolution TEM images were acquired on a JEOL JEM-1400Plus microscope with a thermionic gun (W filament) operated at an acceleration voltage of 120 kV. High-resolution (HR) scanning transmission electron microscopy (STEM) images were acquired on a probe-corrected ThermoFisher Spectra 30–300 (S)TEM operated at 300 kV. Images were acquired on a high-angle annular dark field (HAADF) detector with a current of ≈50 pA. Compositional maps were acquired using Velox, with a probe current of ≈150 pA and rapid rastered scanning of the beam. The energy dispersive X-ray (EDX) signal was collected by a Dual-X system, comprising two detectors, one on either side of the sample, for a total acquisition solid angle of 1.76 Sr. Geometric Phase Analysis (GPA) of the HAADF-HR-STEM images was performed using the commercial Digital Micrograph software package and homemade scripts.[70]

*X-Ray Photoelectron Spectroscopy (XPS)*: XPS analysis was performed on a Kratos Axis Ultra$^{DLD}$ spectrometer using a monochromatic Al K$\alpha$ source (20 mA, 15 kV). Survey scan analyses were carried out over an analysis area of 300 × 700 microns and a pass energy of 160 eV, whereas high resolution analyses were conducted with a pass energy of 10 eV. Specimens for XPS were prepared from concentrated NC solutions, dropped on freshly cleaved highly oriented pyrolytic graphite substrates in a glovebox. The Kratos charge neutralizer system was used on all specimens. Spectra were charge-corrected to the main line of the carbon 1s spectrum (adventitious carbon) set to 284.8 eV. Spectra were analyzed using CasaXPS software (version 2.3.24).[71]

*Inductively Coupled Plasma Optical Emission Spectroscopy (ICP-OES)*: The elemental analysis was carried out via inductively coupled plasma optical emission spectroscopy (ICP-OES) with an iCAP 7600 DUO ICP-OES spectrometer (Thermofisher Scientific). The samples were dissolved in 1 mL of $HNO_3$ overnight and then diluted with 9 mL of Milli-Q water for measurements. The elemental analysis using ICP-OES was affected by a systematic error of ≈5%.

*Raman Spectroscopy*: Raman spectroscopy measurements were performed with a microRaman Invia 1000 (Renishaw, U.K.) using an excitation wavelength of 514 nm, a grating with 2400 lines $cm^{-1}$, and an incident power of 1 mW. An exposure time of 10 s was used for each spectrum, averaging at least 30 spectra for each sample. The samples were held in a nitrogen atmosphere inside a Linkam THMS600 chamber (Linkam Scientific, U.K.). The microscope mounted a Leica 50x long working distance objective. The data were analyzed using the Renishaw Wire 5.6 software.

*Optical Characterization*: The absorption spectrum of nanocrystals in toluene was collected with a Cary 50 UV–vis spectrophotometer. Time-resolved PL measurements were carried out by exciting samples with a ps-pulsed diode laser (Edinburgh EPL405, 70 ps pulses) at an excitation energy of 3.06 eV. PL from the sample was collected with a phototube connected with a Cornerstone 260 1/4m VIS-NIR monochromator (ORIEL) and a single photon counting unit (time resolution ≈400 ps). PLQY measurements were performed using the Edinburgh FLS920 fluorescence spectrometer equipped with an integrating sphere. The samples were excited at 750 nm using the output of continuous xenon lamp. All QDs solutions were diluted to an optical density of ≈0.15 at 750 nm.

*Ultrafast Transient Absorption Spectroscopy (TA)*: TA measurements were carried out with Ultrafast Systems Helios TA spectrometer with a 10 W Hyperion amplified laser operated at 2.142 KHz producing 260 fs pulses at 1030 nm and coupled with an independently tunable APOLLO-Y optical parametric amplifier from the same supplier that produced the excitation pulses at 2.06 eV. The excitation laser (pump beam) was passed through a synchronous chopper phase-locked to the pulse train (1.071 kHz blocking every other pump pulse). NIR light was used as the probe beam. The pump fluence was varied according to the desired value of the average number of excitons per quantum dot in each sample.

*Density Functional Theory Calculations*: Geometry optimizations were performed at the DFT level using the mGGA High-Local-Exchange exchange-correlation functional (HLE17),[72] which has proved to be one of the most accurate functionals for predicting bandgaps,[73] and double-$\zeta$ basis set, as implemented in the CP2K quantum chemistry software package. Relativistic effects were considered through the effective core potentials. The structures were relaxed until the following criteria were met: max_force, $4.5 \times 10^{-4}$ Ha/bohr; rms_force, $3.0 \times 10^{-4}$ Ha/bohr; max_step, $3.0 \times 10^{-3}$ bohr; rms_step, $1.5 \times 10^{-3}$ bohr. The isosurface value used for the charge density plots is $|0.005|$ $(e^-/bohr3)^{1/2}$. The oscillator strengths were calculated using the workflows implemented in the nano-QMFlows package.[74,75]

## Supporting Information

Supporting Information is available from the Wiley Online Library or from the author.

## Acknowledgements

The authors acknowledge Dorwal Marchelli for the support in the optical analyses. Z.L., D.Z., I.I. and L.M. acknowledge funding from the programme MiSE-ENEA under the Grant "Italian Energy Materials Acceleration Platform – IEMAP". The computing resources and the related technical support used for this work have been provided by CRESCO/ENEAGRID High Performance Computing infrastructure and its staff. This study was also supported by IKUR Strategy under the collaboration agreement between Ikerbasque Foundation and BCMaterials on behalf of the Department of Education of the Basque Government. Some of the DFT calculations were carried out at the Donostia International Physics (DIPC) Supercomputing Center, for which the authors acknowledge for the technical and human support. The authors also acknowledge PRACE for awarding access to Leonardo at CINECA, Italy. H.H. and S.B acknowledge support from the European Research Executive Agency (Project DYNAMO, 101072818)

Open access publishing facilitated by Istituto Italiano di Tecnologia, as part of the Wiley - CRUI-CARE agreement.

## Conflict of Interest

The authors declare no conflict of interest.

## Data Availability Statement

The data that support the findings of this study are available from the corresponding author upon reasonable request.

## Keywords

core@shell, III-V semiconductors, indium arsenide, indium phosphide, near infrared

Received: May 24, 2024
Revised: August 5, 2024
Published online: September 10, 2024

[1] T. Müller, J. Skiba-Szymanska, A. B. Krysa, J. Huwer, M. Felle, M. Anderson, R. M. Stevenson, J. Heffernan, D. A. Ritchie, A. J. Shields, *Nat. Commun.* **2018**, *9*, 862.
[2] K. Takemoto, M. Takatsu, S. Hirose, N. Yokoyama, Y. Sakuma, T. Usuki, T. Miyazawa, Y. Arakawa, *J. Appl. Phys.* **2007**, *101*, 081720.
[3] S. Pradhan, F. Di Stasio, Y. Bi, S. Gupta, S. Christodoulou, A. Stavrinadis, G. Konstantatos, *Nat. Nanotechnol.* **2019**, *14*, 72.
[4] P. Geiregat, A. J. Houtepen, L. K. Sagar, I. Infante, F. Zapata, V. Grigel, G. Allan, C. Delerue, D. Van Thourhout, Z. Hens, *Nat. Mater.* **2018**, *17*, 35.
[5] S. Christodoulou, I. Ramiro, A. Othonos, A. Figueroba, M. Dalmases, O. Özdemir, S. Pradhan, G. Itskos, G. Konstantatos, *Nano Lett.* **2020**, *20*, 5909.
[6] J. H. Song, H. Choi, H. T. Pham, S. Jeong, *Nat. Commun.* **2018**, *9*, 4267.
[7] D. Franke, D. K. Harris, O. Chen, O. T. Bruns, J. A. Carr, M. W. B. Wilson, M. G. Bawendi, *Nat. Commun.* **2016**, *7*, 12749.
[8] S. Goossens, G. Navickaite, C. Monasterio, S. Gupta, J. J. Piqueras, R. Pérez, G. Burwell, I. Nikitskiy, T. Lasanta, T. Galán, E. Puma, A. Centeno, A. Pesquera, A. Zurutuza, G. Konstantatos, F. Koppens, *Nat. Photonics* **2017**, *11*, 366.
[9] M. Vasilopoulou, A. Fakharuddin, F. P. García de Arquer, D. G. Georgiadou, H. Kim, A. R. b. Mohd Yusoff, F. Gao, M. K. Nazeeruddin, H. J. Bolink, E. H. Sargent, *Nat. Photonics* **2021**, *15*, 656.
[10] S. Kumar, S. Pradhan, *Adv. Opt. Mater.* **2024**, 2400993.
[11] P. M. Allen, W. Liu, V. P. Chauhan, J. Lee, A. Y. Ting, D. Fukumura, R. K. Jain, M. G. Bawendi, *J. Am. Chem. Soc.* **2010**, *132*, 470.
[12] E. George, M. Pecht, *Microelectron. Reliab.* **2016**, *65*, 1.
[13] C.-O. Gensch, Y. Baron, M. Blepp, O. Deubzer, Öko-Institut eV, Freiburg, Germany **2016**.
[14] Y. Ma, Y. Zhang, W. W. Yu, *J. Mater. Chem. C* **2019**, *7*, 13662.
[15] L. Yang, S. Zhang, B. Xu, J. Jiang, B. Cai, X. Lv, Y. Zou, Z. Fan, H. Yang, H. Zeng, *Nano Lett.* **2023**, *23*, 2443.
[16] D. Battaglia, X. Peng, *Nano Lett.* **2002**, *2*, 1027.

[17] L. Asor, J. Liu, S. Xiang, N. Tessler, A. I. Frenkel, U. Banin, *Adv. Mater.* **2023**, *35*, 2208332.
[18] K. J. Puttlitz, G. T. Galyon, in *Lead-Free Electronic Solders*, Springer, Berlin **2006**.
[19] D. Darwan, L. J. Lim, T. Wang, H. Wijaya, Z.-K. Tan, *Nano Lett.* **2021**, *21*, 5167.
[20] D. Franke, D. K. Harris, L. Xie, K. F. Jensen, M. G. Bawendi, *Angew. Chem.* **2015**, *127*, 14507.
[21] G. Schileo, G. Grancini, *J. Mater. Chem. C.* **2021**, *9*, 67.
[22] M. De Franco, D. Zhu, A. Asaithambi, M. Prato, E. Charalampous, S. Christodoulou, I. Kriegel, L. De Trizio, L. Manna, H. Bahmani Jalali, F. Di Stasio, *ACS Energy Lett.* **2022**, *7*, 3788.
[23] S. Tamang, S. Lee, H. Choi, S. Jeong, *Chem. Mater.* **2016**, *28*, 8119.
[24] T. Kim, S. Park, S. Jeong, *Nat. Commun.* **2021**, *12*, 3013.
[25] H. Bahmani Jalali, L. De Trizio, L. Manna, F. Di Stasio, *Chem. Soc. Rev.* **2022**, *51*, 9861.
[26] T. Sheikh, W. J. Mir, S. Nematulloev, P. Maity, K. E. Yorov, M. N. Hedhili, A.-H. Emwas, M. S. Khan, M. Abulikemu, O. F. Mohammed, O. M. Bakr, *ACS Nano* **2023**, *17*, 23094.
[27] L. K. Sagar, G. Bappi, A. Johnston, B. Chen, P. Todorović, L. Levina, M. I. Saidaminov, F. P. García de Arquer, D.-H. Nam, M.-J. Choi, S. Hoogland, O. Voznyy, E. H. Sargent, *Chem. Mater.* **2020**, *32*, 7703.
[28] X. Peng, J. Wickham, A. P. Alivisatos, *J. Am. Chem. Soc.* **1998**, *120*, 5343.
[29] D. Zhu, H. Bahmani Jalali, G. Saleh, F. Di Stasio, M. Prato, N. Polykarpou, A. Othonos, S. Christodoulou, Y. P. Ivanov, G. Divitini, I. Infante, L. De Trizio, L. Manna, *Adv. Mater.* **2023**, *35*, 2303621.
[30] W. K. Bae, Y.-S. Park, J. Lim, D. Lee, L. A. Padilha, H. McDaniel, I. Robel, C. Lee, J. M. Pietryga, V. I. Klimov, *Nat. Commun.* **2013**, *4*, 2661.
[31] Y.-S. Park, W. K. Bae, T. Baker, J. Lim, V. I. Klimov, *Nano Lett.* **2015**, *15*, 7319.
[32] J. Leemans, D. Respekta, J. Bai, S. Braeuer, F. Vanhaecke, Z. Hens, *ACS Nano* **2023**, *17*, 20002.
[33] V. Srivastava, E. Dunietz, V. Kamysbayev, J. S. Anderson, D. V. Talapin, *Chem. Mater.* **2018**, *30*, 3623.
[34] T.-G. Kim, D. Zherebetskyy, Y. Bekenstein, M. H. Oh, L.-W. Wang, E. Jang, A. P. Alivisatos, *ACS Nano* **2018**, *12*, 11529.
[35] D. Zhu, F. Bellato, H. Bahmani Jalali, F. Di Stasio, M. Prato, Y. P. Ivanov, G. Divitini, I. Infante, L. De Trizio, L. Manna, *J. Am. Chem. Soc.* **2022**, *144*, 10515.
[36] A. Aharoni, T. Mokari, I. Popov, U. Banin, *J. Am. Chem. Soc.* **2006**, *128*, 257.
[37] Y. W. Cao, U. Banin, *J. Am. Chem. Soc.* **2000**, *122*, 9692.
[38] V. Grigel, D. Dupont, K. De Nolf, Z. Hens, M. D. Tessier, *J. Am. Chem. Soc.* **2016**, *138*, 13485.
[39] J. P. Zimmer, S.-W. Kim, S. Ohnishi, E. Tanaka, J. V. Frangioni, M. G. Bawendi, *J. Am. Chem. Soc.* **2006**, *128*, 2526.
[40] R. Tietze, R. Panzer, T. Starzynski, C. Guhrenz, F. Frenzel, C. Würth, U. Resch-Genger, J. J. Weigand, A. Eychmüller, *Part. Part. Syst. Charact.* **2018**, *35*, 1800175.
[41] R. Xie, K. Chen, X. Chen, X. Peng, *Nano Res.* **2008**, *1*, 457.
[42] M. J. Enright, D. Jasrasaria, M. M. Hanchard, D. R. Needell, M. E. Phelan, D. Weinberg, B. E. McDowell, H.-W. Hsiao, H. Akbari, M. Kottwitz, M. M. Potter, J. Wong, J.-M. Zuo, H. A. Atwater, E. Rabani, R. G. Nuzzo, *J. Phys. Chem. C* **2022**, *126*, 7576.
[43] L. K. Sagar, G. Bappi, A. Johnston, B. Chen, P. Todorović, L. Levina, M. I. Saidaminov, F. P. García de Arquer, S. Hoogland, E. H. Sargent, *Chem. Mater.* **2020**, *32*, 2919.
[44] H. Wijaya, D. Darwan, K. R. G. Lim, T. Wang, K. H. Khoo, Z.-K. Tan, *Chem. Mater.* **2019**, *31*, 2019.
[45] V. Srivastava, V. Kamysbayev, L. Hong, E. Dunietz, R. F. Klie, D. V. Talapin, *J. Am. Chem. Soc.* **2018**, *140*, 12144.
[46] X. Zhao, L. J. Lim, S. S. Ang, Z.-K. Tan, *Adv. Mater.* **2022**, *34*, 2206409.
[47] H. Wijaya, D. Darwan, X. Zhao, E. W. Y. Ong, K. R. G. Lim, T. Wang, L. J. Lim, K. H. Khoo, Z.-K. Tan, *Adv. Funct. Mater.* **2020**, *30*, 1906483.
[48] K. R. G. Lim, D. Darwan, H. Wijaya, Z. C. Lim, J. Shanmugam, T. Wang, L. J. Lim, W. H. Ang, Z.-K. Tan, *Adv. Mater. Interfaces* **2020**, *7*, 2000920.
[49] S.-W. Kim, J. P. Zimmer, S. Ohnishi, J. B. Tracy, J. V. Frangioni, M. G. Bawendi, *J. Am. Chem. Soc.* **2005**, *127*, 10526.
[50] R. Xie, X. Peng, *Angew. Chem., Int. Ed.* **2008**, *47*, 7677.
[51] Y. W. Cao, U. Banin, *Angew. Chem., Int. Ed.* **1999**, *38*, 3692.
[52] A. Milnes, A. Polyakov, *Mater. Sci. Eng., B.* **1993**, *18*, 237.
[53] G. E. Cragg, A. L. Efros, *Nano Lett.* **2010**, *10*, 313.
[54] G. A. Beane, K. Gong, D. F. Kelley, *ACS Nano* **2016**, *10*, 3755.
[55] F. Pietra, L. De Trizio, A. W. Hoekstra, N. Renaud, M. Prato, F. C. Grozema, P. J. Baesjou, R. Koole, L. Manna, A. J. Houtepen, *ACS Nano* **2016**, *10*, 4754.
[56] R. F. Ubbink, G. Almeida, H. Iziyi, I. du Fossé, R. Verkleij, S. Ganapathy, E. R. H. van Eck, A. J. Houtepen, *Chem. Mater.* **2022**, *34*, 10093.
[57] R. Yadav, Y. Kwon, C. Rivaux, C. Saint-Pierre, W. L. Ling, P. Reiss, *J. Am. Chem. Soc.* **2023**, *145*, 5970.
[58] M. D. Tessier, K. De Nolf, D. Dupont, D. Sinnaeve, J. De Roo, Z. Hens, *J. Am. Chem. Soc.* **2016**, *138*, 5923.
[59] A. Faust, Y. Amit, U. Banin, *J. Phys. Chem. Lett.* **2017**, *8*, 2519.
[60] V. Srivastava, E. M. Janke, B. T. Diroll, R. D. Schaller, D. V. Talapin, *Chem. Mater.* **2016**, *28*, 6797.
[61] M. J. Seong, O. I. Mićić, A. J. Nozik, A. Mascarenhas, H. M. Cheong, *Appl. Phys. Lett.* **2003**, *82*, 185.
[62] K. Boldt, *Nano Futures* **2022**, *6*, 012003.
[63] H. Van Avermaet, P. Schiettecatte, S. Hinz, L. Giordano, F. Ferrari, C. Nayral, F. Delpech, J. Maultzsch, H. Lange, Z. Hens, *ACS Nano* **2022**, *16*, 9701.
[64] L. González, J. M. García, R. García, F. Briones, J. Martínez-Pastor, C. Ballesteros, *Appl. Phys. Lett.* **2000**, *76*, 1104.
[65] T. Mano, A. Ohtake, T. Kuroda, *Phys. Status Solidi* **2024**, *221*, 2300767.
[66] Q. Zheng, J. Wang, F. Huang, Z. Huang, S. Tian, Q. Chen, Y. Pei, K. Zheng, J. Tian, *ACS Energy Lett.* **2024**, *9*, 2358.
[67] J. Llusar, I. du Fossé, Z. Hens, A. Houtepen, I. Infante, *ACS Nano* **2024**, *18*, 1563.
[68] Z. Liu, R. Pascazio, L. Goldoni, D. Maggioni, D. Zhu, Y. P. Ivanov, G. Divitini, J. L. Camarelles, H. B. Jalali, I. Infante, L. De Trizio, L. Manna, *J. Am. Chem. Soc.* **2023**, *145*, 18329.
[69] E. L. Rosen, R. Buonsanti, A. Llordes, A. M. Sawvel, D. J. Milliron, B. A. Helms, *Angew. Chem., Int. Ed.* **2012**, *51*, 684.
[70] A. K. Gutakovskii, A. L. Chuvilin, S. A. Song, *Bull. Russ. Acad. Sci.: Phys.* **2007**, *71*, 1426.
[71] N. Fairley, V. Fernandez, M. Richard-Plouet, C. Guillot-Deudon, J. Walton, E. Smith, D. Flahaut, M. Greiner, M. Biesinger, S. Tougaard, D. Morgan, J. Baltrusaitis, *Appl. Surf. Sci. Adv.* **2021**, *5*, 100112.
[72] P. Verma, D. G. Truhlar, *J. Phys. Chem. C.* **2017**, *121*, 7144.
[73] P. Borlido, J. Schmidt, A. W. Huran, F. Tran, M. A. L. Marques, S. Botti, *npj Comput. Mater.* **2020**, *6*, 96.
[74] F. Zapata, L. Ridder, J. Hidding, C. R. Jacob, I. Infante, L. Visscher, *J. Chem. Inf. Model.* **2019**, *59*, 3191.
[75] F. Iannone, F. Ambrosino, G. Bracco, M. D. Rosa, A. Funel, G. Guarnieri, S. Migliori, F. Palombi, G. Ponti, G. Santomauro, P. Procacci, presented at 2019 International Conference on High Performance Computing & Simulation (HPCS), Dublin, Ireland, July, **2019**.